Chinese Journal of
POLYMER SCIENCE

RESEARCH ARTICLE

https://doi.org/10.1007/s10118-026-3636-3
Chinese J. Polym. Sci. **2026**, *44*, 2691–2703

Evolutionary Characteristics of Linear Free-radical Polymerization Behavior under Gradient Condition

Hui Li[a*], Bing-Bing Pan[a], Yi-Yi Zhang[a], Wen Li[a], Zi-Jian Xue[a], Zhen-Bin Chen[a], and Hong Liu[b]

[a] *School of Material Science and Engineering, LanZhou University of Technology, Lanzhou 730050, China*
[b] *Key Laboratory of Theoretical Chemistry of Environment, Ministry of Education, School of Environment, South China Normal University, Guangzhou 510006, China*

Electronic Supplementary Information

Abstract This study investigates the evolution of free-radical polymerization under spatially graded conditions by constructing a position-dependent reaction probability model. Given the strong temperature dependence of thermal initiators, spatial temperature variations significantly affect both local monomer reactivity and the macroscopic evolution of polymer structures. Understanding this coupling is crucial for designing gradient-controlled synthesis strategies. The dissipative particle dynamics (DPD) method was employed to investigate free radical polymerization under gradient temperature conditions. Increasing ΔT enhances spatial heterogeneity: high-temperature regions form dense networks with lower molecular weights (M_n and M_w) due to rapid initiation and frequent termination. In contrast, low-temperature regions yield higher molecular weights and expanded chain conformations ($<R_g^2>$) resulting from longer radical lifetimes. These structural differences further govern pore evolution: porosity decreases rapidly and reaches lower final values in high-temperature zones, while low-temperature regions exhibit delayed evolution but higher final porosity. This study demonstrates that the precise control of polymer growth orientation, molecular weight distribution, and porous morphology can be achieved by incorporating gradient conditions, thereby establishing a new paradigm for the targeted synthesis of gradient functional materials.

Keywords Free radical polymerization; Gradient structure; Dissipative particle dynamics; Polymerization kinetics

Citation: Li, H.; Pan, B. B.; Zhang, Y. Y.; Li, W.; Xue, Z. J.; Chen, Z. B.; Liu, H. Evolutionary characteristics of linear free-radical polymerization behavior under gradient condition. *Chinese J. Polym. Sci.* **2026**, *44*, 2691–2703.

INTRODUCTION

Free radical polymerization (FRP), one of the most widely used and widely applied chain growth polymerization techniques, remains a cornerstone of polymer synthesis owing to its broad monomer compatibility, mild reaction conditions, high tolerance to impurities, and excellent process flexibility.[1–3] Although recent studies have focused more on controlled radical polymerization (CRP),[4–6] conventional FRP is still widely used in various application fields, including coatings,[7–10] biomedical materials,[11–14] absorbent materials[15–18] and stimuli-responsive polymers.[19–22] In FRP-based polymer synthesis, researchers typically select different initiation methods—such as thermal,[23–27] photoinduced[28–30] or redox initiation[31–33] —depending on the type of initiator used. Among these, thermal decomposition of initiators is the most common approach,[34] and temperature serves as a critical external factor influencing the entire polymerization process.

However, most existing studies have been carried out under uniform temperature conditions, and experimental investigations on polymerization behavior in non-uniform or gradient temperature fields remain limited. In practice, non-uniform temperature fields are not uncommon. For example, the heat released during polymerization[34,35] and the limited efficiency of heat transfer[36,37] often lead to temperature gradients within the system. These gradients, in turn, cause local variations in molecular weight and cross-linking density, ultimately imparting anisotropic or gradient structures to the resulting materials. Lloyd *et al.*[36] demonstrated through numerical simulations that modulation of reaction kinetics and heat transfer in frontal polymerization (FP) enables internal feedback control of thermal gradients, allowing the spontaneous regulation of morphological, chemical, optical, and mechanical properties of materials. Ye *et al.*[37] utilized the synergistic effects of spontaneous oxygen penetration into a mixed solution and heat transfer from an external source to achieve bottom-up gradient polymerization, producing ordered gradient hydrogels with selective pollutant enrichment capability. Therefore, exploring free radical polymerization behavior under temperature-gradient conditions is of great significance for understanding and controlling polymer structure formation.

* Corresponding author, E-mail: lihuidhg@lut.edu.cn
Received January 31, 2026; Accepted February 26, 2026; Published online July 1, 2026

In uniform temperature fields, the kinetics of free radical polymerization has been extensively studied,[34] The temperature dependence of the elementary reactions—initiation, propagation, and termination—follows the Arrhenius relationship. The activation energy of initiation (E_d) is much higher than that of propagation (E_p) and termination (E_t), making it more sensitive to temperature variations. Meanwhile, the rate constant of initiation (k_d) is significantly smaller than those of propagation (k_p) and termination (k_t), rendering the initiation step the rate-determining stage of the overall polymerization process. This kinetic feature makes free radical polymerization highly sensitive to temperature. Kinoshita *et al*.[38] reported that poly(acrylic acid) (PAA) could be obtained with a conversion of 60.3% in only 5.2 seconds without any catalyst, by briefly heating an aqueous solution of acrylic acid (AA) with potassium persulfate (KPS). This observation suggests that, in a continuous gradient temperature field, spatial asymmetry in the initiation reaction may induce subsequent gradient propagation and termination processes, ultimately leading to the formation of spatially structured polymers along the temperature direction. However, both experimental and simulation studies on this topic remain scarce. The variation of key parameters such as molecular weight (M_n, M_w) and chain packing density under continuous temperature gradients are still unclear and require systematic investigation.

Direct experimental observation of the spatial evolution of polymerization reactions under a temperature gradient is challenging. Therefore, many researchers have employed computer simulations—especially coarse-grained methods—to investigate the resulting polymer structures,[4,39–41] In this work, we employ the dissipative particle dynamics (DPD) method to systematically explore the spatial evolution of free-radical polymerization behavior driven by a gradient temperature field. The influence of the spatial temperature gradient on the polymerization kinetics is realized by constructing a simulation system containing monomer and initiator particles, in which a temperature-dependent reaction probability function is introduced. During the simulation, initiator decomposition and subsequent polymerization occur differently in regions with varying temperatures, leading to spatial variations in polymerization rates. Consequently, structural parameters such as molecular weight distribution and packing density evolve along the temperature gradient. By comparing the results under different temperature gradients and conversion rates, we elucidate the mechanism of spatial differentiation in polymer structures induced by temperature gradients. This work provides fundamental insights into the formation of gradient structures and offers new strategies for designing and preparing gradient hydrogels and other functional polymeric materials.

SIMULATION METHODS AND MODEL

Dissipative Particle Dynamics

Dissipative Particle Dynamics (DPD) is a mesoscale simulation method first proposed by Hoogerbrugge and Koelman in 1992.[42] The DPD approach is particularly suitable for modeling polymer systems, as it introduces a bead-spring representation that effectively captures the conformational changes and dynamic behaviors of molecular chains. Although some atomic-level details are lost during the coarse-graining process, the thermodynamic and hydrodynamic properties of the system can still be accurately reproduced at the mesoscopic scale. This advantage makes DPD a powerful tool for investigating polymer solutions, self-assembly processes, and interfacial phenomena.[43,44] The motion of all particles in DPD follows the Newtonian equations of motion:

$$\frac{\mathrm{d}\mathbf{r}_i}{\mathrm{d}t} = \mathbf{v}_i, \quad \frac{\mathrm{d}\mathbf{v}_i}{\mathrm{d}t} = \mathbf{f}_i \tag{1}$$

where $\mathbf{r}_i$, $\mathbf{v}_i$ and $\mathbf{f}_i$ denote the position, velocity, and total force of particle i with mass m at time t, respectively. In the DPD framework, the total force acting on a particle consists of three components: conservative, dissipative, and random (or stochastic) forces, which can be expressed as follows:

$$\mathbf{F}_{ij}^{\mathrm{C}} = a_{ij} w^{\mathrm{C}}(r_{ij}) \hat{\mathbf{r}}_{ij} \tag{2}$$

$$\mathbf{F}_{ij}^{\mathrm{D}} = -\gamma w^{\mathrm{D}}(\mathbf{r}_{ij})(\mathbf{v}_{ij} \cdot \hat{\mathbf{r}}_{ij}) \hat{\mathbf{r}}_{ij} \tag{3}$$

$$\mathbf{F}_{ij}^{\mathrm{R}} = \sigma' w^{\mathrm{R}}(r_{ij}) \zeta_{ij} \Delta t^{-1/2} \hat{\mathbf{r}}_{ij} \tag{4}$$

where a_{ij} is the interparticle repulsion coefficient, r_{ij} is the interparticle distance, $\hat{\mathbf{r}}_{ij}$ is the corresponding unit vector, γ denotes the dissipation coefficient, $\mathbf{v}_{ij}$ is the relative velocity between particles i and j, σ is the noise amplitude, ζ_{ij} is a random variable with zero mean and unit variance. $w^{\mathrm{C}}(r_{ij})$, $w^{\mathrm{D}}(r_{ij})$ and $w^{\mathrm{R}}(r_{ij})$ represent the weight functions for the conservative, dissipative, and random forces, respectively, when $r_{ij} < r_c$, the conservative weight function is defined as $w^{\mathrm{C}}(r_{ij}) = (1 - r_{ij}/r_c)$, otherwise, it equals zero, r_c is the cutoff radius for interparticle interactions. The system satisfies the fluctuation-dissipation theorem (FDT),[45] which ensures thermodynamic equilibrium and relates the dissipative and random forces as follows:

$$\sigma'^2 = 2\gamma k_B T, \quad w^{\mathrm{D}}(r_{ij}) = [w^{\mathrm{R}}(r_{ij})]^2 \tag{5}$$

where k_B is the Boltzmann constant, $w^{\mathrm{D}}(r_{ij})$ and $w^{\mathrm{R}}(r_{ij})$ chose the classical form:[46]

$$w^{\mathrm{D}}(r_{ij}) = [w^{\mathrm{R}}(r_{ij})]^2 = \begin{cases} \left(1 - \frac{r_{ij}}{r_c}\right)^2, & r_{ij} < r_c \\ 0, & r_{ij} \geq r_c \end{cases} \tag{6}$$

For convenience of numerical calculation, the simulation parameters are reduced to dimensionless units, where $r_c = k_B T = m = 1.0$. The Groot–Warren Velocity–Verlet (GW–VV) integration algorithm[43,47] was employed to integrate Newton's equations of motion:

$$\mathbf{r}_i(t + \Delta t) = \mathbf{r}_i(t) + \Delta t \mathbf{v}_i(t) + \frac{1}{2}(\Delta t)^2 \mathbf{f}_i(t) \tag{7}$$

$$\tilde{\mathbf{v}}_i(t + \Delta t) = \mathbf{v}_i(t) + \lambda \Delta t \mathbf{f}_i(t) \tag{8}$$

$$\mathbf{f}_i(t + \Delta t) = \mathbf{f}_i[\mathbf{r}(t + \Delta t), \tilde{\mathbf{v}}(t + \Delta t)] \tag{9}$$

$$\mathbf{v}_i(t + \Delta t) = \mathbf{v}_i(t) + \frac{1}{2}\Delta t(\mathbf{f}_i(t) + \mathbf{f}_i(t + \Delta t)) \tag{10}$$

where $\tilde{\mathbf{v}}$ represents the predicted velocity, velocity prediction parameter λ was set to 0.65, and the integration time step was $\Delta t = 0.04$, the unit of time was defined as $\tau = \sqrt{m r_c^2 / k_B T} = 1$. A finitely extensible nonlinear elastic potential function model (FENE) was used to describe the bonding interactions between molecular chain segments in the DPD simulations:[48]

https://doi.org/10.1007/s10118-026-3636-3

$$U_{FENE}(r) = -\frac{1}{2}kR_0^2\ln[1-\left(\frac{r}{R_0}\right)^2], \ r < R_0 \quad (11)$$

where bond stiffness coefficient k was set to 30.0, and the maximum bond extension R_0 was set to 1.5σ, where σ represents the reduced unit of length.

Gradient Temperature Field

In this work, a simulation box with dimensions of $40 \times 40 \times 100$ was constructed, with periodic boundary conditions applied in the x and y directions, while the z direction was kept non-periodic to preserve the spatial gradient imposed along this direction. Applying periodicity along z would artificially connect the high- and low-gradient regions and thus disrupt the physical consistency of the gradient field. A linear temperature gradient (ΔT) was established along the z axis, as illustrated in Fig. 1. This gradient remained stable throughout the reaction and serves as a simplified model to systematically investigate the effects of temperature gradients on free radical polymerization. A dissipative particle dynamics (DPD) approach was employed to reveal the underlying mechanisms of the gradient effect within this idealized temperature field. It should be noted that temperature distributions in real systems are often more complex, typically non-uniform and dynamically evolving over time. Although the present model assumes a linear gradient, the methodology is broadly applicable. In future studies, if transient temperature field data from experiments or multiphysics simulations are available, they can be directly incorporated into the current DPD framework, enabling accurate predictions of polymerization behavior under more realistic and complex gradient conditions.

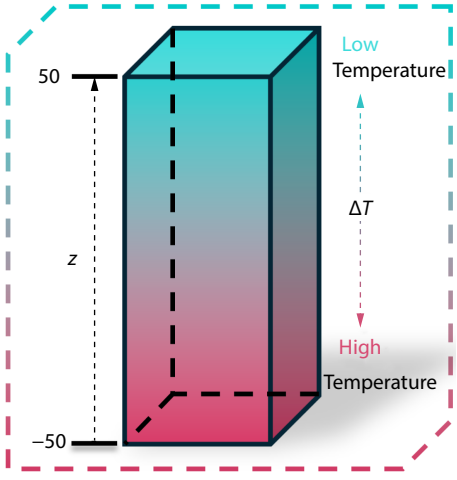

Fig. 1 Temperature gradient schematic.

The temperature gradient is denoted as ΔT, representing the temperature difference between the two ends of the z axis of the simulation box. With reference to typical experimental temperature ranges for hydrogel preparation *via* free-radical polymerization,[37,49,50] six values of ΔT were considered in this work: 0, 6, 12, 18, 24, and 30 °C. A linear temperature profile was adopted along the z axis, with the midpoint of the box (z=0) maintained at a uniform reference temperature, T_{mid}.

Modeling Free Radical Polymerization in a Gradient Temperature Field

In this simulation, the initiator, radicals, and monomers involved in the free radical polymerization were coarsely grained into individual bead particles, with polymer chains represented as a series of connected beads. At each simulation step, an initiator particle (I) is converted into a radical (R_{ad}) with probability P_r^d, Although initiators are typically difunctional molecules that generate two radicals *via* thermal, photochemical, or electron-transfer decomposition, in this work, the initiator is assumed to be monofunctional, producing only one radical[4,51]; Polymerization occurs with probability P_r^p when the distance between a radical and a monomer (r_{RM}) satisfies $r_{RM} \leq r_{cut} = 1.0\sigma$, the monomer is then converted into a propagating radical (R_{ad}*), while the original radical becomes part of the growing polymer chain. Particles incorporated into polymer chains are considered inert and do not participate in subsequent reactions. If the distance between two on-chain radicals (*i.e.*, propagating radicals), r_{RR}, satisfies $r_{RR} \leq r_{cut} = 1.0\sigma$, a disproportionation termination reaction could occur with probability P_r^t, forming a termination radical (R_{te}), however, this process is not considered in the present model. A more detailed description of the explicit free radical polymerization model is provided in Fig. S1 (in the electronic supplementary information, ESI).

The reaction probability parameter was determined based on the Arrhenius reaction rate constant, k. In free radical polymerization, the rate constants typically satisfy $k_d << k_p << k_t$, with k_p approximately 6–8 orders of magnitude larger than k_d, and k_t about 4–6 orders of magnitude larger than k_p.[34] These differences arise from the distinct activation energies of the three radical reactions: the initiation reaction (decomposition of the initiator) has the highest activation energy E_d, approximately 126–165 kJ/mol; the chain propagation reaction has an intermediate activation energy E_p of 20–40 kJ/mol, and the termination reaction has the lowest activation energy E_t, about 8–20 kJ/mol. Consequently, the rate constants exhibit different temperature sensitivities.[34]

P_r^d (T_{mid}) was set to 5×10^{-6}, Fig. 2(a) shows the time evolution of initiator particle conversion under this probability. Repeatable stability validation of the initiation is shown in Fig. S2 (in ESI).

Then, a chain-growth reaction model, as shown in Fig. 3, was constructed to determine the relationship between P_r^p and k_p: A single radical particle was initially placed in the simulation box, while the remaining volume was filled with monomer particles (for clarity, monomer particles are not shown in Fig. 3). In this model, the radical particle reacts with monomer particles under five different polymerization probabilities, P_r^p = 0.002, 0.004, 0.006, 0.008 and 0.01, with three independent simulations performed for each probability. To avoid the influence of high steric hindrance on chain growth kinetics, the chain growth rate (R_p) was calculated only when the monomer conversion was below 10%. Subsequently, the value of k_p was obtained according to the kinetic formula for chain growth in free radical polymerization:[34]

$$R_p = k_p[M][R_{ad}^*] \quad (12)$$

where [M] represents the monomer concentration and [R_{ad}*] is the propagating radical concentration. The calculation results

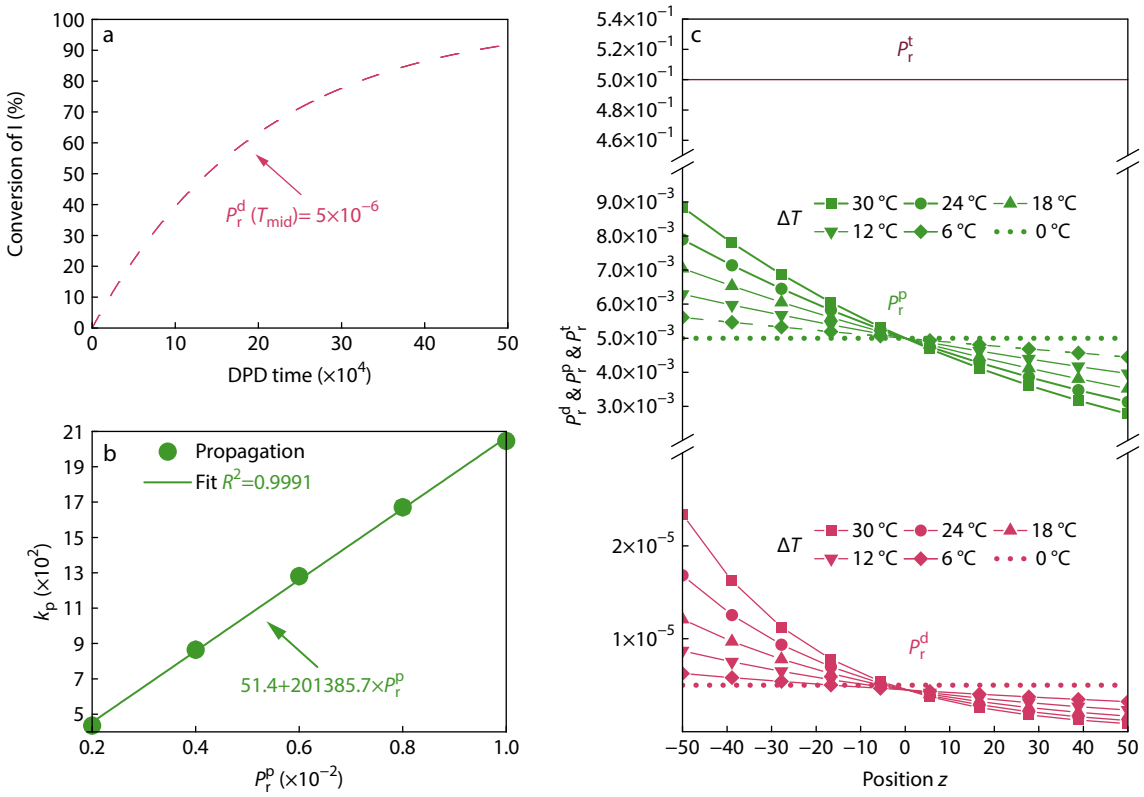

Fig. 2 (a) Initiator conversion curve at T_{mid}; (b) P_r^d-k_p relationship; (c) Probability settings.

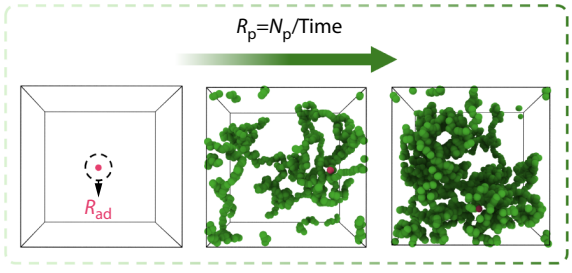

Fig. 3 Determination of the propagation k_p.

are shown in Fig. 2(b), indicating a linear relationship between P_r^p and k_p, moreover, we verified that the box dimensions do not affect this linear relationship (Fig. S3 in ESI). P_r^p (T_{mid}) was set to 0.005.

Since both P_r^d-k_d and P_r^p-k_p relationships are linear, the following settings were adopted in this model with reference to experimental kinetic parameters: P_r^d increases threefold for every 10 °C, P_r^p increases threefold for every 30 °C, and P_r^t is assumed to be temperature-independent and fixed at 0.5. Reaction-capable particles in the system were assigned specific reaction probabilities according to the temperature corresponding to their *z*-coordinate positions. Here, P_r^d, P_r^p and P_r^t were scaled to reduce the ratios between k_d, k_p and k_t in order to avoid excessive computational cost, while maintaining the condition $k_d < k_p < k_t$. Fig. 2(c) shows the variation of P_r^d, P_r^p and P_r^t with the *z*-coordinate for different ΔT. In this model, the scaling relationship between P_r^d and k_d is linear. The initiator concentration, c_I, was fixed in the simulation at $c_M \times 0.2\%$, where c_M is the monomer concentration.

Quantitative Characterization of the Structure

To characterize the specific effect of the temperature gradient on structural evolution during free radical polymerization, several structural parameters were statistically analyzed under different gradient conditions. All statistical results were obtained from three mutually independent simulations with different random seeds, and the corresponding mean values and standard deviations were evaluated to ensure the robustness of the observed trends. First, the distributions of the number of chain-forming particles and the number of molecular chains along the temperature gradient direction (*z* axis) were obtained by calculating the center-of-mass coordinates of the molecular chains. Subsequently, the distributions of number-averaged molecular weight (M_n), weight-averaged molecular weight (M_w), polymer dispersity index (PDI), and the mean-square radius of gyration ($<R_g^2>$) were analyzed to reveal the gradient-induced differences in molecular size. M_n and M_w are defined as follows:

$$M_n = \frac{\sum_i N_i M_i}{\sum_i N_i}, M_w = \frac{\sum_i N_i M_i^2}{\sum_i N_i M_i} \quad (13)$$

where N_i is the number of chains with molecular weight M_i, PDI = M_w/M_n. The calculation of $<R_g^2>$ is given by Eq. (15):

$$< R_g^2 >= \left(\frac{1}{N}\right) \times \sum_{i=1}^{N} (\boldsymbol{r}_i - \boldsymbol{r}_{cm})^2 \quad (14)$$

where *N* is the total number of particles in the polymer chain, $\boldsymbol{r}_i$ is the position vector of the i^{th} particle, and $\boldsymbol{r}_{cm}$ is the center-of-mass position vector of the polymer chain, which is defined as:

$$r_{cm} = \left(\frac{1}{N}\right) \times \sum_{i=1}^{N} \boldsymbol{r}_i \quad (15)$$

To further investigate the gradient characteristics of the pore distribution, the simulation box along the *z* axis was divided into slices with a thickness of 1σ and a sampling interval of 10σ (Fig. 4a), and the porosity (Defined as the proportion of blank space in a top-down two-dimensional diagram: porosity = S_{blank} / S_{slice}) of each slice was calculated. The system was also divided into two regions, "Up" (low-temperature region) and "Down" (high-temperature region) (Fig. 4b), to quantitatively compare the differences in the above-mentioned parameters—including the number of chain-forming particles, molecular chains, molecular weight, and porosity—between the high- and low-temperature regions. The differences between these two regions were used to assess the significance of the gradient effect, the "Up/Down" or "Down/Up" of the above properties was simultaneously computed to quantify the gradient.

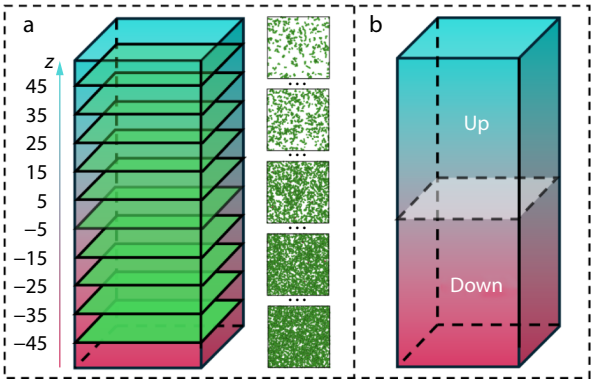

Fig. 4 (a) Schematic of slices used to characterize pore gradients; (b) Schematic of the division of the "Up" and "Down" Regions.

RESULTS AND DISCUSSION

Number Distribution of Chain-forming Particles and Molecular Chains

The simulated snapshots of the free radical polymerization process under different temperature gradients (ΔT) are shown in Fig. 5. C_{on} represents the conversion rate of monomer. As ΔT increases, the gradient characteristics of the polymerization reaction become more pronounced: the reaction rate is significantly higher in the high-temperature region along the *z* axis. Even when the monomer conversion reaches 90%, a marked difference in molecular chain packing density along the *z* axis remains observable.

Fig. 6(a) shows the distribution of the number of molecular chains along the *z* axis under different ΔT conditions. In all cases, the number of molecular chains near the edges of the simulation box is lower than in neighboring regions. This is mainly because periodic boundary conditions were not applied along the *z* axis (the temperature gradient direction) to avoid unnatural interactions between particles at the boundaries. As a result, the degrees of freedom at the boundaries are limited, making it difficult for molecular chains to fully stretch; chains tend to grow inward, shifting their center of mass toward the interior, which leads to a lower stacking density at the boundaries. Fig. 6(a) also illustrates the morphology of molecular chains in the boundary and intermediate regions at 90% monomer conversion (chains are colored to distinguish them and visualized in two dimensions to show stacking density). The molecular chains at the boundary are few and spatially constrained, whereas those in the intermediate region interpenetrate, resulting in a higher stacking density. As ΔT increases, the gradient in the distribution of molecular chain numbers becomes more pronounced. This is attributed to the higher rate of radical generation in the high-temperature region (Fig. S4 in ESI), which promotes the formation of new chains and leads to a rapid increase in chain number in this region, whereas chain growth in the low-temperature region is slower. Consequently, the number of molecular chains in the high-temperature region exceeds that in the low-temperature region.

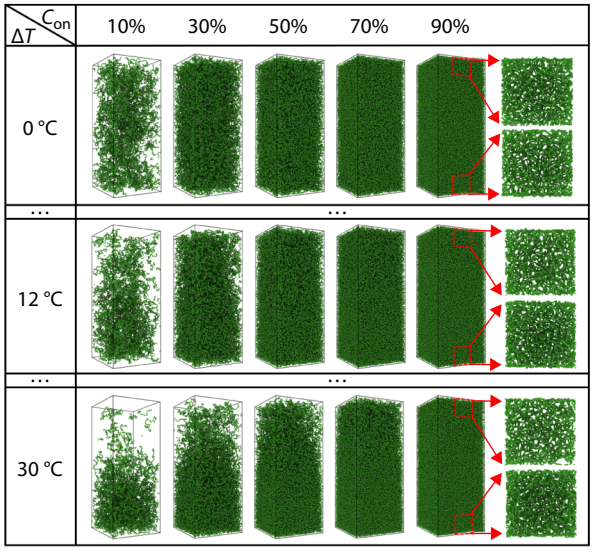

Fig. 5 Snapshots of free radical polymerization growth processes with different ΔT in this simulation.

Fig. 6(b) shows the distribution of the number of chain-forming particles along the *z* axis under different ΔT conditions. Similar to the distribution of molecular chains, the number of chain-forming particles near the boundaries is slightly lower than in neighboring regions under all ΔT conditions, due to the reduced stacking density at the boundaries. However, this effect is limited and does not significantly affect the overall distribution trend. As ΔT increases, the distribution becomes increasingly skewed: the number of chain-forming particles in the high-temperature region rises more rapidly because of the higher rate of radical generation and the enhanced probability of chain growth reactions, resulting in a greater number of chain-forming particles in the high-temperature region compared to the low-temperature region.

Fig. 6(c) shows the Down/UP of the number of molecular chains versus the number of chain-forming particles for different ΔT during the reaction process. As the monomer conversion increased, both ratios gradually decreased under all non-zero ΔT conditions. The ratio of chain-forming particles decreased the fastest, approaching 1.0 in all cases at 90% conversion, whereas the ratio of molecular chain numbers decreased more slowly, remaining around 1.8 at ΔT = 30 °C This

https://doi.org/10.1007/s10118-026-3636-3

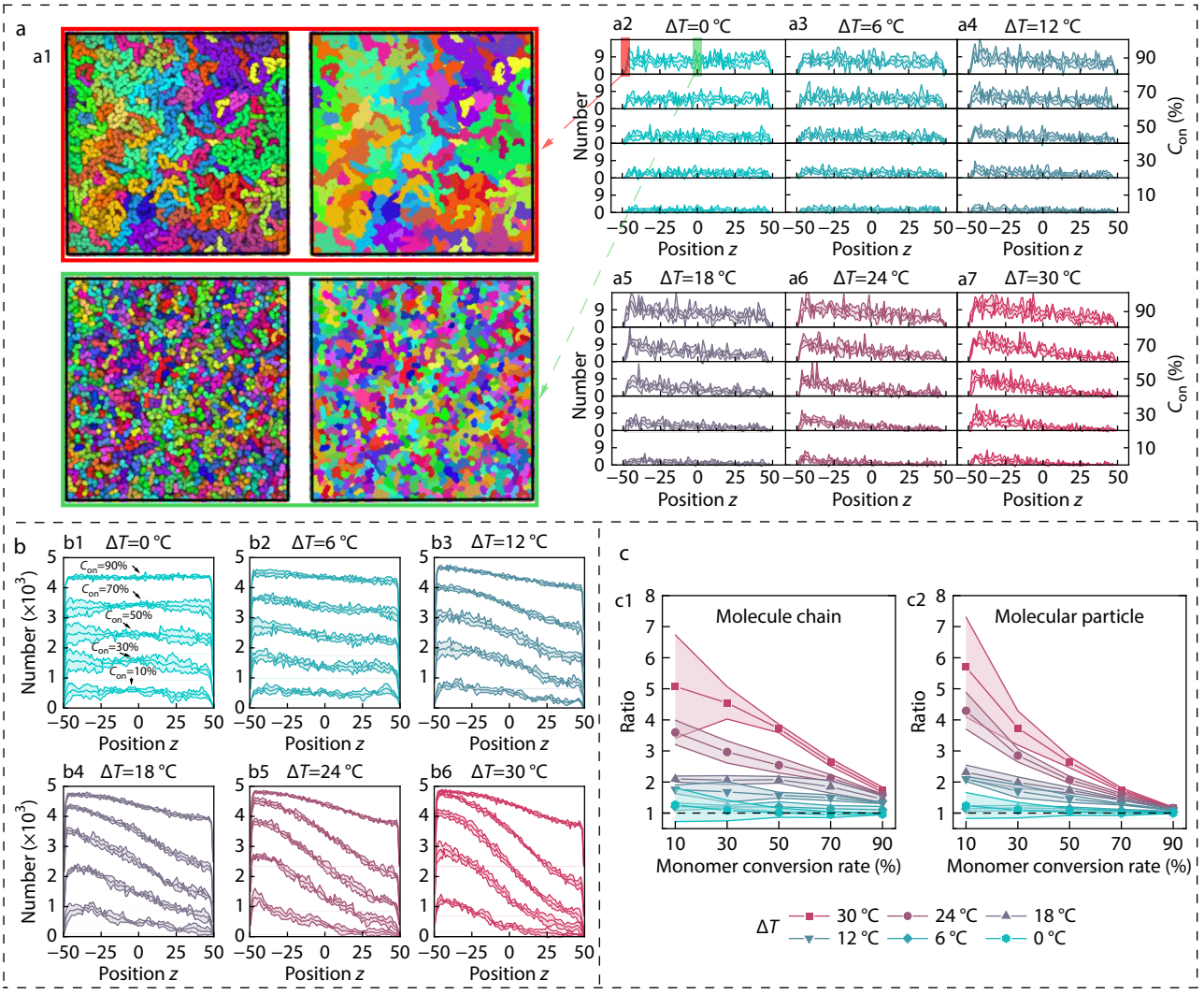

Fig. 6 (a) Distribution of the number of molecular chains with different Δ*T* along the *z* axis direction during the reaction process and morphological differences between the edge and middle positions; (b) Number distribution of chain-forming particles with different Δ*T* along the *z* axis direction during the reaction process; (c) Down/Up of the number of molecular chains versus the number of chain-forming particles for different Δ*T* during the reaction process.

difference can be attributed to the following factors: the number of molecular chains is mainly governed by the rate of radical generation, which becomes more pronounced in both the high- and low-temperature regions as Δ*T* increases. In contrast, the number of chain-forming particles is influenced not only by radical generation but also by chain growth and cross-linking reactions. Although there is a difference in cross-linking probability between the high- and low-temperature regions, the difference in radical conversion probability is relatively small. Additionally, molecular chains formed in the high-temperature region can migrate to the low-temperature region and continue to grow, leading to a faster decrease in the ratio of chain-forming particles compared to the ratio of molecular chains. Moreover, the total amount of monomer in the system is limited, and monomer consumption in the low-temperature region can exceed 80% when the overall conversion reaches 90%, which ultimately causes the ratio to converge toward 1.0, Fig. S7 (in ESI) displays the histogram distribution of both along the *z*-axis at this point.

Distribution of Molecular Weight of Polymers

Fig. 7 illustrates the variations of the weight-averaged molecular weight (M_w), number-averaged molecular weight (M_n), and polymer dispersity index (PDI) in the high-temperature (Down) and low-temperature (Up) regions under different Δ*T* during the polymerization process. The results show that M_w and M_n in both regions increase continuously with conversion for all Δ*T* values, while the growth rate of M_w is higher than that of M_n, leading to a gradual rise in PDI. When the monomer conversion reaches approximately 50%, the growth of M_w and M_n slows down, and M_n even shows a slight decrease, whereas PDI continues to increase slowly. At 90% conversion, the PDI of all groups remains around 2.0, consistent with the typical characteristics of disproportionation-terminated free radical polymerization.[34] By comparing different Δ*T* conditions, it is observed that with increasing Δ*T*, M_w and M_n in the high-temperature region (Down) exhibit a decreasing trend, particularly when the monomer conversion exceeds 30%. In contrast, the molecular weights in the low-temperature region (Up) continue to in-

https://doi.org/10.1007/s10118-026-3636-3

crease. At 90% conversion, the M_w and M_n in the low-temperature region are significantly higher than those in the high-temperature region for all non-zero ΔT cases (except $\Delta T = 0$ °C and 6 °C). These results indicate that with increasing ΔT, molecular chains in the low-temperature region tend to grow longer, while those in the high-temperature region become shorter, highlighting the enhanced polarization of molecular chain length along the temperature gradient, Fig. S8 (in ESI) presents the results after further subdividing the *z*-axis distribution range.

Fig. 8 illustrates the UP/Down of the M_w versus the M_n for different ΔT during the reaction process. In the early stage of the reaction (monomer conversion<30%), the number of molecular chains in the low-temperature region under larger ΔT conditions is smaller, and their molecular weights are lower, resulting in both M_w and M_n being lower than those in the high-temperature region, and consequently, a smaller ratio. However, as the monomer conversion exceeds 30%, M_w and M_n in the higher ΔT groups gradually increase. When the conversion reaches 90%, the magnitudes of M_w and M_n strictly follow the order of ΔT—that is, the larger the ΔT, the higher the ratio—which is the exact opposite of the trend observed at the initial reaction stage.

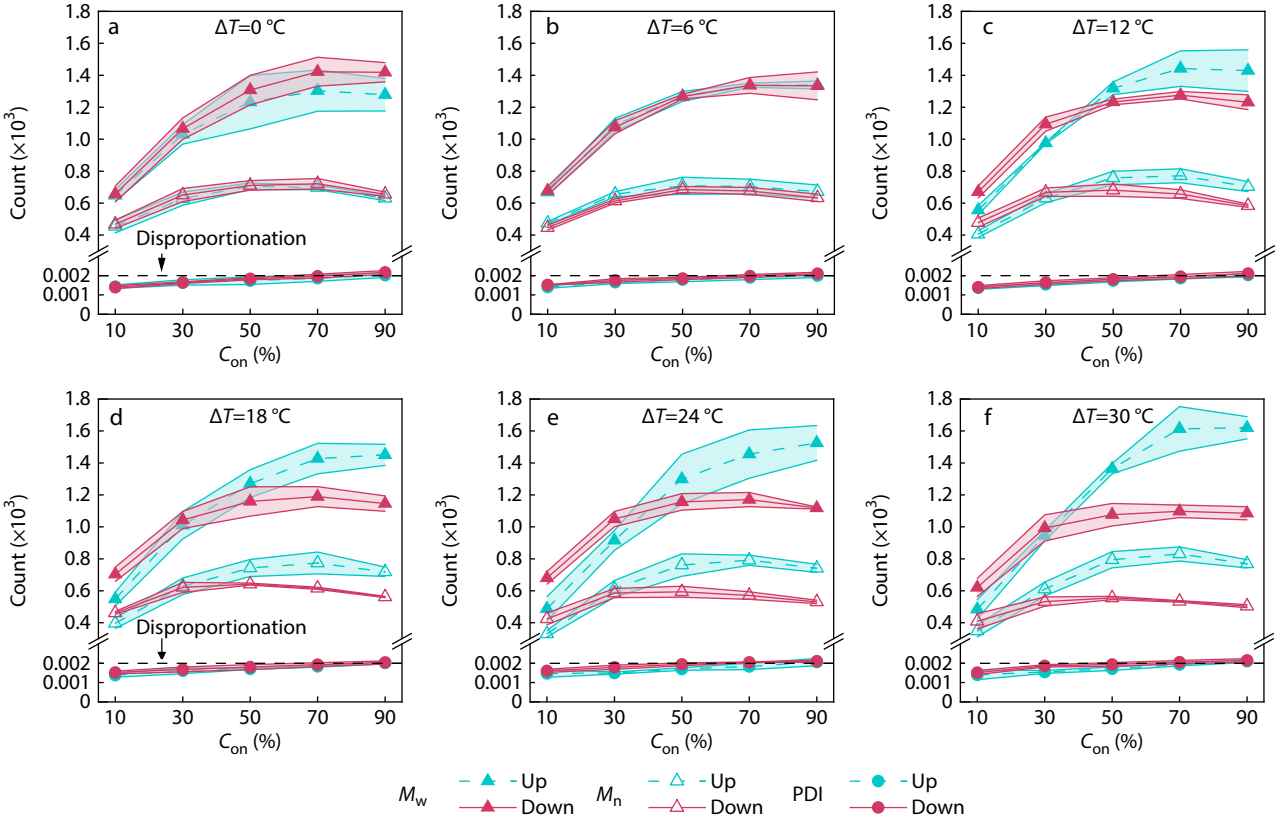

Fig. 7 M_w, M_n and PDI in the Up and Down region during the reaction process at different ΔT: (a) 0 °C; (b) 6 °C; (c) 12 °C; (d) 18 °C; (e) 24 °C; (f) 30 °C.

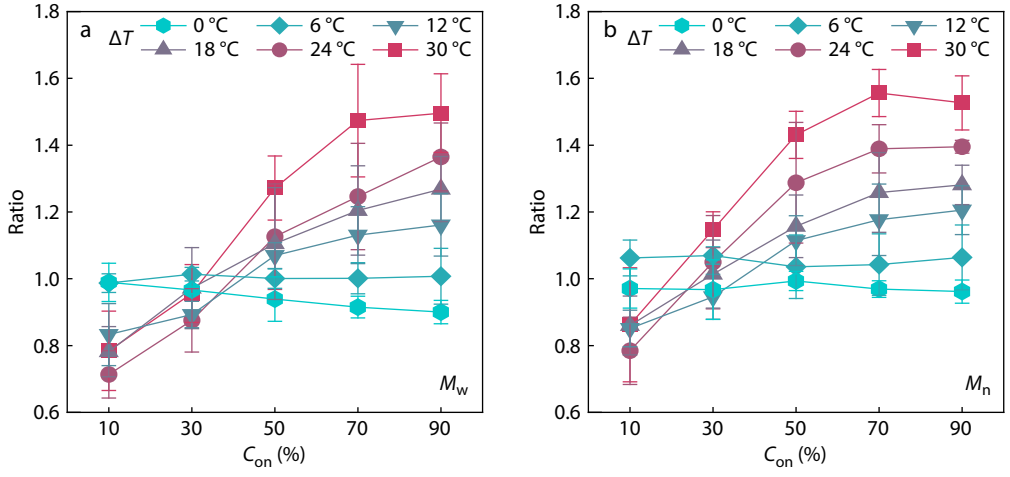

Fig. 8 Up/Down of (a) M_w and (b) M_n during the reaction process at different ΔT.

https://doi.org/10.1007/s10118-026-3636-3

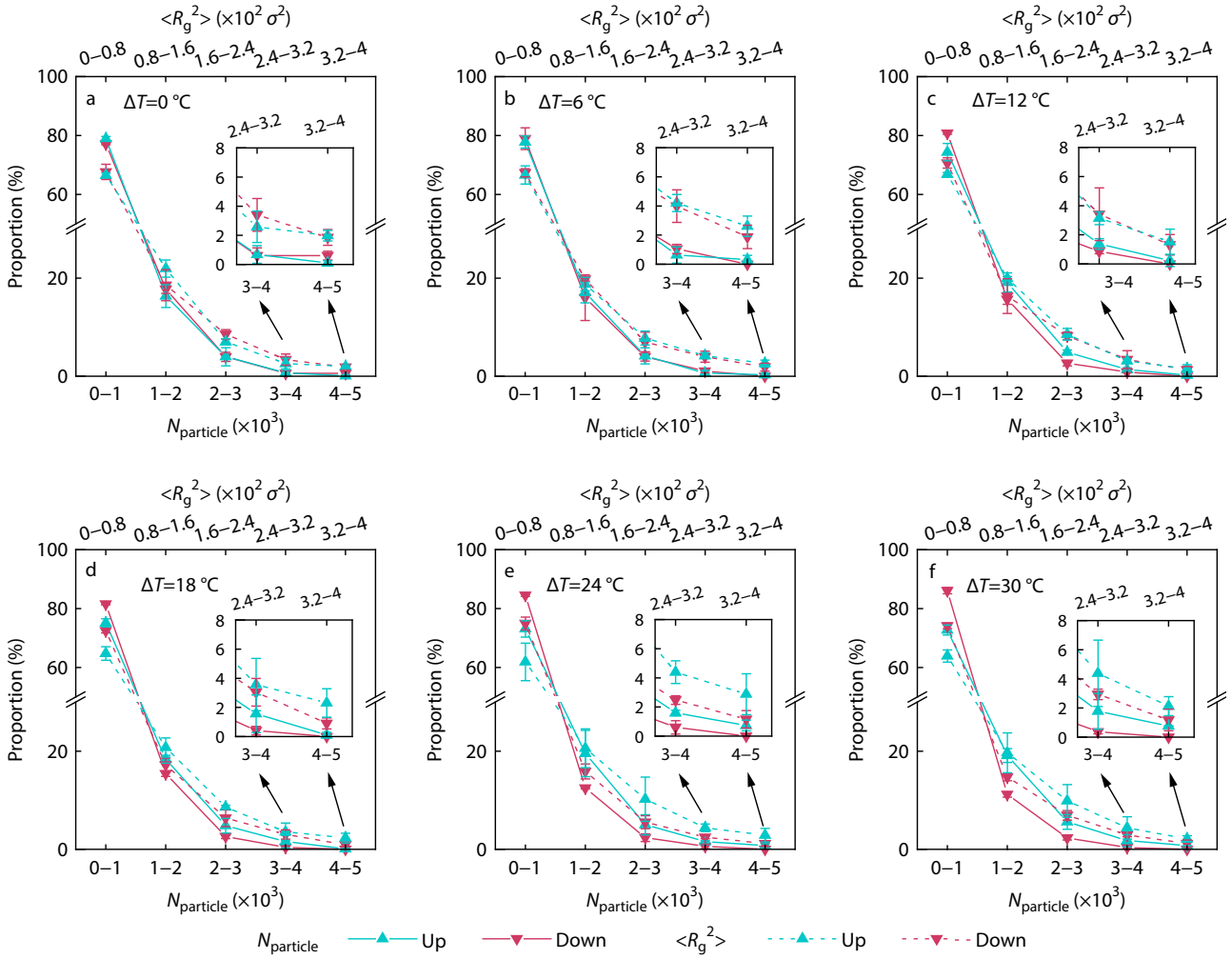

Fig. 9 Distribution of $N_{particle}$ and $<R_g^2>$ for molecular chains at 90% monomer conversion with different ΔT: (a) 0 °C; (b) 6 °C; (c) 12 °C; (d) 18 °C; (e) 24 °C; (f) 30 °C.

Fig. 9 presents the distributions of chain-forming particle numbers ($N_{particle}$) and $<R_g^2>$ of molecular chains under different ΔT at a monomer conversion of 90%. In the non-gradient system (ΔT=0 °C), molecular chains containing ≤1000 chain-forming particles dominate in both the low-temperature (UP) and high-temperature (Down) regions, accounting for about 80%, while chains with $<R_g^2> \leq 80\sigma^2$ represent roughly 67%, indicating a system mainly composed of short chains with a typical Flory-type molecular weight distribution. As ΔT increases, the high-temperature region shows an increasing proportion of short and compact chains, whereas the low-temperature region exhibits the opposite trend. For instance, at ΔT=30 °C, the fraction of chains with ≤1000 particles rises to about 85% and those with $<R_g^2> \leq 80\sigma^2$ to about 75% in the high-temperature region, while these proportions decrease to about 75% and about 65%, respectively, in the low-temperature region. Correspondingly, the fraction of longer and more extended chains increases in the low-temperature region but decreases in the high-temperature region. In particular, the proportion of chains containing 1000–2000 particles increases from about 17% to about 20% in the low-temperature region while dropping to about 10% in the high-temperature region, and when $\Delta T \geq 12$ °C, chains with more than 1000 particles and $<R_g^2> > 80\sigma^2$ become more prevalent in the low-temperature region. At ΔT=30 °C, chains with ≥ 3000 chain-forming particles appear exclusively in the low-temperature region, leading to a pronounced broadening of the molecular size and conformational distributions. Overall, the evolution of $<R_g^2>$ closely follows that of the chain-forming particle number, the "Up/Down" indicators for both are also consistent (Fig. S9 in ESI), demonstrating that an increasing temperature gradient promotes the formation of longer and more extended molecular chains in the low-temperature region.

Fig. 10 shows the evolution of the numbers of propagating radicals (R_{ad}*) and terminated radicals (R_{te}) in the low-temperature (Up) and high-temperature (Down) regions under different ΔT. As ΔT increases, both R_{ad}* and R_{te} populations in the high-temperature region (Down) increase, while those in the low-temperature region (Up) decrease. This is mainly because higher temperatures accelerate the generation rate of radicals (R_{ad}), which promotes the accumulation of R_{ad}* and termination reactions, thereby facilitating the enrichment of

https://doi.org/10.1007/s10118-026-3636-3

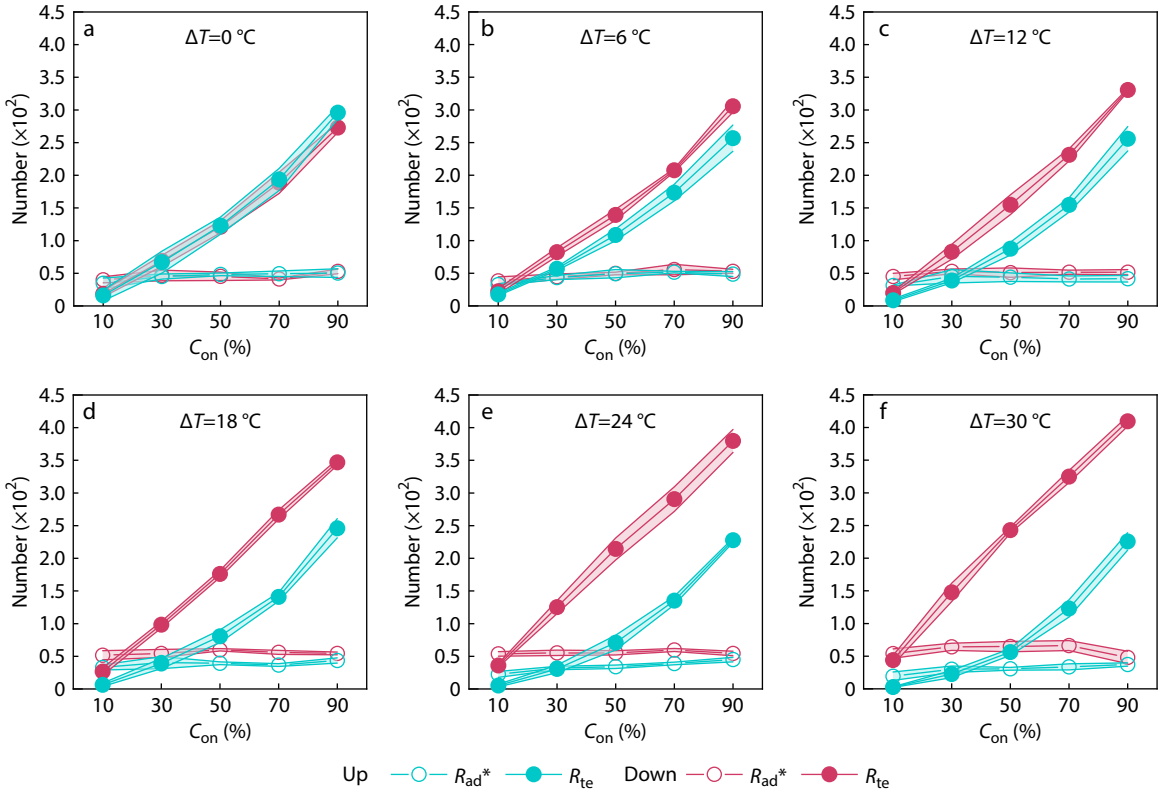

Fig. 10 Number of propagating radical R_{ad}* and terminated radical R_{te} during the reaction process at different Δ*T*: (a) 0 °C; (b) 6 °C; (c) 12 °C; (d) 18 °C; (e) 24 °C; (f) 30 °C.

short polymer chains. In contrast, at lower temperatures, the radical generation rate is slower, the competition among radicals for monomers is reduced, and the termination probability decreases, which favors continuous chain propagation. This mechanism also explains why, with increasing Δ*T*, the number of molecular chains in the high-temperature region increases, whereas both the M_w and M_n molecular weights are lower than those in the low-temperature region. Moreover, at larger temperature gradients (Δ*T*=18, 24, and 30 °C), the number of R_{ad}* in the low-temperature region continuously increases, while that in the high-temperature region remains at a lower level when the overall monomer conversion reaches 90%, resulting in the smallest difference in R_{ad}* populations between the two regions. Comparative analysis reveals that, although the total time required to reach 90% overall monomer conversion is nearly identical under different Δ*T* conditions (Fig. S3 in ESI), an increase in Δ*T* leads to higher initiator and monomer conversions in the high-temperature region and lower conversions in the low-temperature region, showing a more pronounced polarization. For example, at Δ*T*=30 °C and an overall monomer conversion of 70%, the local conversions of monomer and initiator reach 90% and 80% in the high-temperature region, but only 60% and 40% in the low-temperature region, respectively. At this stage, the reduced number of initiator and monomer particles in the high-temperature region results in a lower generation rate of R_{ad} and fewer monomer particles available for propagation, causing a decrease in R_{ad}* due to termination. Conversely, although the generation rate of R_{ad} is slower in the low-temperature region, the smaller number of R_{ad}* leads to longer radical lifetimes, and the relatively sufficient monomer supply enables continuous accumulation of R_{ad}*. This behavior is further confirmed by the temporal evolution of propagating radicals shown in Fig. S5 (in ESI).

Fig. 11 shows the Changes in R_{ad}* and R_{te} Up/Down with reaction progress at different Δ*T*. With increasing Δ*T*, both ratios exhibit a gradual overall increase. For the R_{ad}* ratio, a continuous decrease is observed during the reaction process when Δ*T* is 24 °C and 30 °C. In particular, at Δ*T*=30 °C, the initial ratio exceeds 3.0 and finally decreases to about 1.24. This variation can be divided into three distinct stages: In the first stage (C_{on}<30%), the ratio drops rapidly. This is attributed to the fast radical generation rate in the high-temperature region, accompanied by frequent termination reactions, while part of the propagating chains grow into the low-temperature region, resulting in the migration of some R_{ad}* to the low-temperature side. Since radicals in the low-temperature region have longer lifetimes and slower chain-growth rates, the R_{ad}* ratio decreases sharply. In the second stage (C_{on} of 30%–70%), the ratio decreases slowly, as new chain formation and chain termination in both regions gradually reach a dynamic equilibrium. In the third stage (C_{on} of 70%–90%), the ratio again decreases rapidly. The high-temperature region becomes depleted of monomers and exhibits higher chain packing density, which suppresses new chain formation while termination reactions continue, leading to a decrease in the number of R_{ad}*. In contrast, the low-temperature region still maintains a monomer-rich environment, allowing the accumulation of R_{ad}*, thereby accelerating the decline of the R_{ad}*

https://doi.org/10.1007/s10118-026-3636-3

ratio. For the R_{te} ratio, it remains relatively high at the early stage of the reaction (*e.g.*, around 17 at ΔT=30 °C) and continuously decreases thereafter. All nonzero ΔT conditions show the same downward trend, with the ratio in the ΔT=30 °C condition ultimately dropping to approximately 1.82.

Pore Distribution

Based on the previous analysis of particle numbers and molecular weights along the *z* axis under different temperature gradients (ΔT), it can be inferred that the system structure, particularly the chain stacking density, exhibits spatial variation along the temperature gradient. To further quantify this effect, the porosity along the *z* axis was analyzed to examine gradient differences in structural compactness. Porosity was calculated as the area fraction of void space excluding the molecular chains in each slice. Fig. 12 presents the evolution of porosity along the *z* axis during the reaction under different ΔT. When ΔT=0 °C, the *z*-direction porosity shows no specific fluctuation and decreases from approximately 75% to 6% as the reaction proceeds. With increasing ΔT, the curves become increasingly skewed: the porosity in the high-temperature region (z<0) continuously decreases, while that in the low-temperature region (z > 0) gradually increases. For example, at ΔT=30 °C, the porosity at z = –45 drops from 60% to 2.45%, whereas at z=45, it decreases from

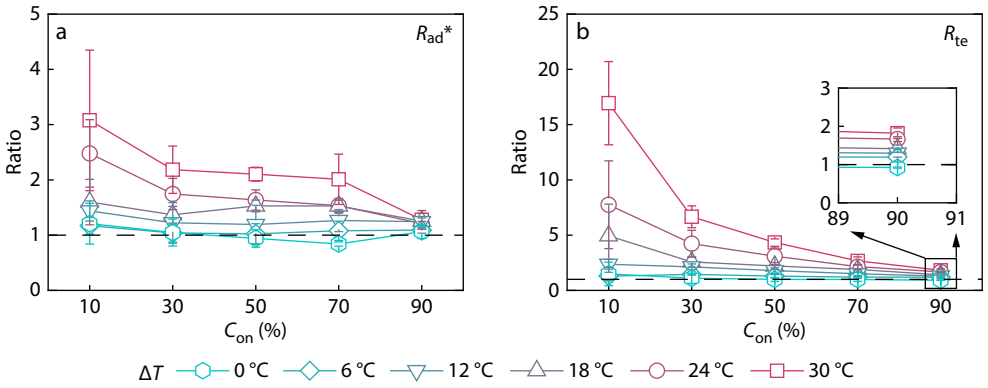

Fig. 11 Changes in Up/Down of (a) R_{ad}* and (b) R_{te} during the reaction progress at different ΔT.

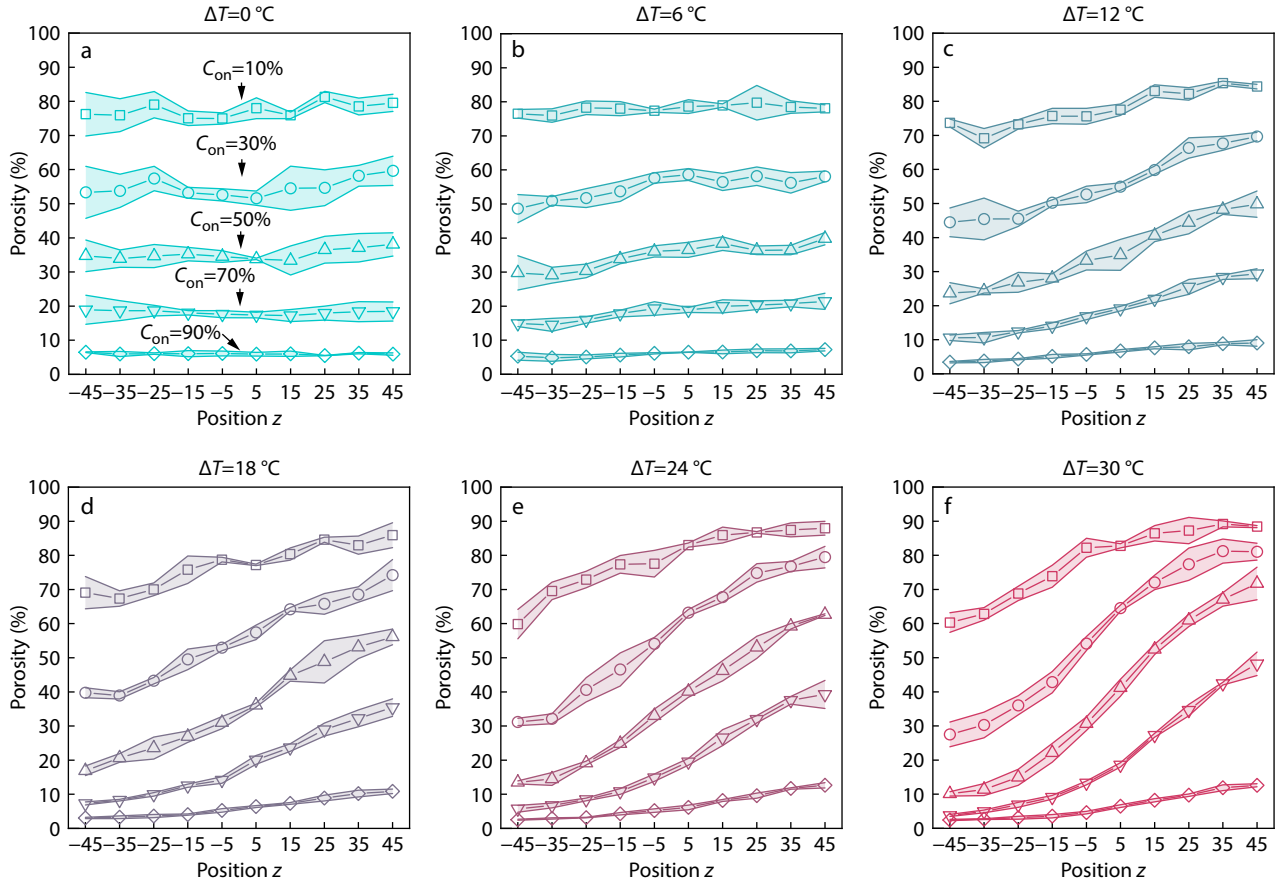

Fig. 12 Porosity during the reaction process at different ΔT: (a) 0 °C; (b) 6 °C; (c) 12 °C; (d) 18 °C; (e) 24 °C; (f) 30 °C.

https://doi.org/10.1007/s10118-026-3636-3

85% to 12.6%. Notably, during the monomer conversion range of 70%–90%, the porosity at z = –45 decreases slightly from 3.7% to 2.45%, showing a small change of just over 1%, while the low-temperature region shows a much larger decrease from 50% to 10%. This trend becomes more pronounced with increasing ΔT. In other words, at larger ΔT (*e.g.*, 30 °C), the porosity in the low-temperature region exhibits a delayed decline, with its peak change occurring at later reaction stages (overall monomer conversion rate of 70%), whereas the high-temperature region shows a rapid decrease at earlier stages, with porosity reaching near-stable levels when the overall monomer conversion is 70%.

Fig. 13 shows the Up/Down of average porosity for different ΔT during the reaction process. The overall ratio increases with increasing ΔT. During the reaction, the ratio rises continuously for all ΔT until the monomer conversion reaches approximately 70%, after which, except for ΔT=0 °C and 6 °C, the ratios for the remaining ΔT decrease. This behavior arises because, before 70% conversion, the number of molecular chains in the high-temperature region increases faster than in the low-temperature region, and the abundance of short chains facilitates denser packing, leading to a faster decrease in porosity. In contrast, the low-temperature region contains longer chains with stronger entanglement interactions, resulting in looser packing. Beyond 70% conversion, according to Fig. S4 (in ESI), the monomer consumption rate is significantly higher in the high-temperature zone. For instance, at ΔT=30 °C, consumption in this zone reaches approximately 88%, whereas it remains below 60% in the low-temperature zone. chain growth in the high-temperature region slows and the structure stabilizes, limiting further porosity reduction, while new chains in the low-temperature region continue to fill voids, causing the ratio to decline. This effect becomes more pronounced with increasing ΔT.

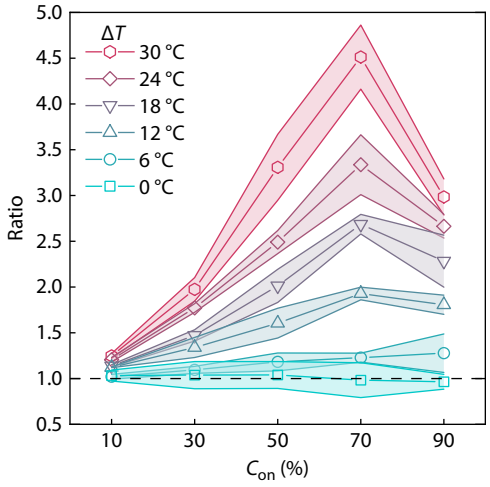

Fig. 13 Up/Down of average porosity for different ΔT during the reaction process.

CONCLUSIONS

This study employed DPD simulations to investigate the spatiotemporal regulatory role of temperature gradients (ΔT) in free radical polymerization and their control over the resulting polymer structures. By analyzing the spatial distribution of chain-forming particles and polymer chains, molecular weight, chain size, and porosity evolution under varying ΔT, we demonstrate that increasing the temperature gradient significantly enhances structural heterogeneity across the system. This heterogeneity stems from distinct kinetic and diffusive behaviors induced by the spatial variation in temperature. In the high-temperature region, accelerated initiation rates promote rapid radical generation and monomer consumption, leading to a higher concentration of terminated radicals. This process yields a larger population of shorter chains and a denser network with reduced porosity. In contrast, low-temperature regions exhibit slower reactivity but prolonged radical lifetimes, which favors extended chain growth and results in higher molecular weight polymers with more expanded conformations and increased porosity. The competition between reaction and diffusion leads to an earlier evolution of structural parameters such as porosity in high-temperature zones, whereas development in cooler regions is delayed. Overall, this work establishes a programmable strategy for internal polymer architectures through controlled external temperature fields. By applying a defined temperature gradient during polymerization, we achieve precise spatial control over chain distribution, molecular weight, and pore morphology. These findings not only advance the mechanistic understanding of polymerization under non-uniform conditions but also provide a theoretical and computational foundation for the rational design of gradient-functional materials, including gradient hydrogels, separation membranes, and tissue engineering scaffolds.

Conflict of Interests

The authors declare no interest conflict.

Electronic Supplementary Information

Electronic supplementary information (ESI) is available free of charge in the online version of this article at http://doi.org/10.1007/s10118-026-3636-3.

Data Availability Statement

The data that support the findings of this study are available from the corresponding author upon reasonable request.

ACKNOWLEDGMENTS

This work was financially supported by the National Natural Science Foundation of China (No. 22463006); Qinzhou District Science and Technology Major Special Project in Tianshui City (No. 2024-NCKJG-4929).

REFERENCES

1 Liu, S. The future of free radical polymerizations. *Chem. Mater.* **2024**, *36*, 1779–1780.

Graphical Abstract

Evolutionary Characteristics of Linear Free-radical Polymerization Behavior under Gradient Condition

Hui Li, Bing-Bing Pan, Yi-Yi Zhang, Wen Li, Zi-Jian Xue, Zhen-Bin Chen, and Hong Liu

LanZhou University of Technology; South China Normal University

Increasing ΔT intensifies spatial heterogeneity in free-radical polymerization. High-temperature regions promote rapid initiation and termination, yielding lower M_n and M_w, whereas low-temperature regions produce higher molecular weights, larger $\langle R_g^2 \rangle$, and slower porosity reduction.

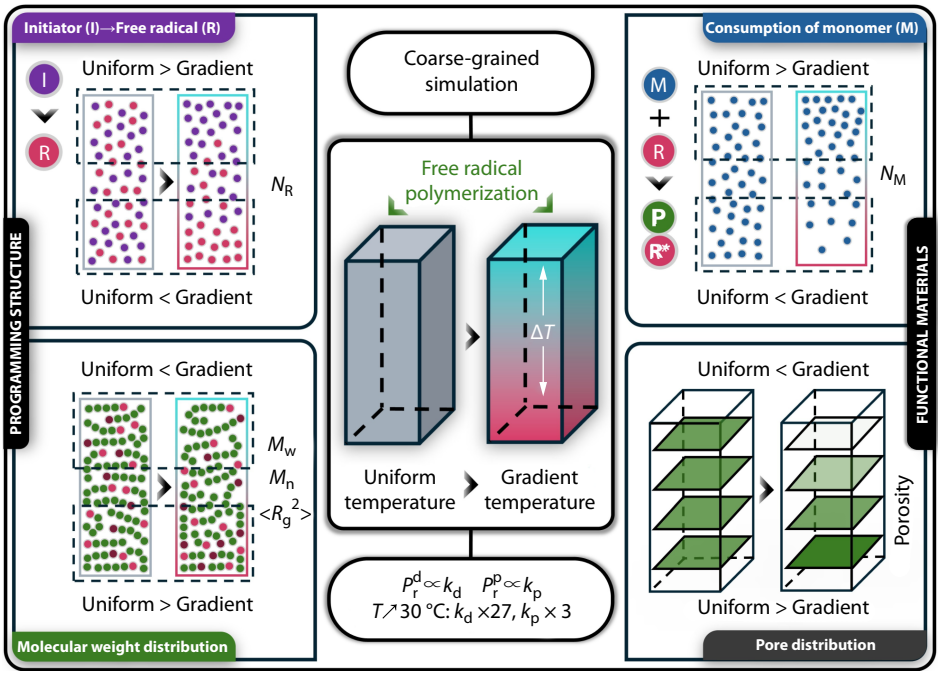

Chinese J. Polym. Sci. 2026, 44, 2691–2703 *https://doi.org/10.1007/s10118-026-3636-3*

2 Truong, N. P.; Jones, G. R.; Bradford, K. G. E.; Konkolewicz, D.; Anastasaki, A. A comparison of raft and atrp methods for controlled radical polymerization. *Nat. Rev. Chem.* **2021**, *5*, 859–869.
3 Nesvadba, P. in *Encyclopedia of radicals in chemistry, biology and materials*, John Wiley & Sons, Bologna, **2012**, p. 2099
4 Zhang, Z.; Krajniak, J.; Dookhith, A. Z.; Tian, Y.; Sachar, H. S.; Marioni, N.; Duncan, T. J.; Liu, J.; Sanoja, G. E.; Ganesan, V. Topology and mechanical properties of polymer networks formed under free radical and atom transfer radical polymerizations. *Macromolecules* **2025**, *58*, 3168–3187.
5 Mantzara, D.; Whitfield, R.; Wang, H. S.; Truong, N. P.; Anastasaki, A. Ultrafast thermal raft depolymerization at higher solid contents. *ACS Macro Lett.* **2025**, *14*, 235–240.
6 Kayanuma, M. A theoretical study of radical formation mechanisms in pet-raft polymerization using porphyrins as photoredox catalysts. *J. Phys. Chem. A* **2025**, *129*, 2718–2724.
7 Li, X.; Shi, J.; Kong, C.; Li, C.; Wang, H.; Jiang, S.; Li, Y. Photoinitiator-grafted polymer coating enable various hydrogels with strong resistance to both drying and swelling. *Chem. Eng. J.* **2024**, *480*, 147937.
8 Zhang, Y.; Xie, Q.; Pan, J.; Ma, C.; Zhang, G. Strong-adhesion and nonfouling self-generating zwitterionic janus hydrogel paint. *Chem. Eng. J.* **2024**, *485*, 149959.
9 Wen, S.; Xu, Y.; Fan, L.; Peng, B.; Zhang, J.; Zhang, Q.; Pang, Y.; Deng, Y.; Zou, Y. Hydrophilic coating of membrane by uv-induced radical and cationic curing of photosensitive resins: lower shrinkage, smoother surface and better anti-fouling performance. *Prog. Org. Coat.* **2024**, *195*, 108666.
10 Yao, M.; Wei, Z.; Li, J.; Guo, Z.; Yan, Z.; Sun, X.; Yu, Q.; Wu, X.; Yu, C.; Yao, F.; Feng, S.; Zhang, H.; Li, J. Microgel reinforced zwitterionic hydrogel coating for blood-contacting biomedical devices. *Nat. Commun.* **2022**, *13*, 5339.
11 Wei, M.; Wang, H.; Chen, C.; Fei, G.; Yang, D.; Li, K.; Wang, M.; Yang, X.; Li, N.; Song, L.; Yang, M.; Wang, Z. Conductive, adhesive, and biocompatible hydrogel sensor based on zwitterionic for effective wound healing and monitoring. *Chem. Eng. J.* **2025**, *506*, 160235.
12 Zhu, H.; Wang, C.; Yang, Y.; Ma, H.; Fan, X.; Zhang, Y.; Dai, Z.; Cai, R.; Qian, K. High-strength mechanically gradient hydrogels *via* physical crosslinking for tendon-mimetic tissue repair. *npj Flex Electron.* **2025**, *9*, 53.
13 Quan, Z.; Wang, X.; Zheng, K.; Wen, Y.; Lin, J.; Cui, M. Synthesis of novel composite hydrogel based on Carboxymethyl

Cellulose/Acrylamide/β-Cyclodextrin for drug delivery. *Int. J. Biol. Macromol.* **2025**, *287*, 138387.
14 Hashem, M. S.; Sobh, R. A.; Fahim, A. M.; Elsayed, G. H. Alginate sulfonamide hydrogel beads for 5-fluorouracil delivery: antitumor activity, cytotoxicity assessment, and theoretical investigation. *Int. J. Biol. Macromol.* **2024**, *282*, 136573.
15 Makhado, E. Preparation of carboxymethyl cellulose-based silica hydrogel nanocomposite for methylene blue and malachite green dyes adsorption from aqueous solution. *Surf. Interfaces* **2025**, *56*, 105699.
16 Lakshmi Priya, A.; Subhapriya, P.; Jenisha, S.; Murali Krishnan, M.; Dhanapal, V. Experimental and theoretical investigation of allylated chitosan and acrylic acid-based smart polymer hydrogel for the removal of brilliant green from aqueous media. *Int. J. Biol. Macromol.* **2025**, *289*, 138814.
17 Chaurasiya, A.; Pande, P. P.; Shankar, R.; Khare, P.; Kumar, P.; Yadav, N. K.; Dey, K. K. Synthesis and characterization of chemically functionalized novel smart guar gum xanthate based hydrogel: swelling, isotherm, kinetics, thermodynamic and reusability studies. *J. Phys. Chem. Solids* **2025**, *200*, 112584.
18 Nair, A.; Kumawat, Y. K.; Choudhary, S.; Nath, J.; Sharma, K.; Rasool, T.; Sharma, V.; Kumar, V. Malachite green dye adsorption from wastewater using pine gum-based hydrogel: kinetic and thermodynamic studies. *J. Mol. Struct.* **2024**, *1295*, 136671.
19 Song, L.; Wang, Z.; Chen, S.; Shen, Y.; Yin, J.; Wang, R. Phytic acid-induced gradient hydrogels for highly sensitive and broad range pressure sensing. *Adv. Mater.* **2025**, *37*, 2417978.
20 Zhang, X.; Aziz, S.; Zhu, Z. Tough and fast thermoresponsive hydrogel soft actuators. *Adv. Mater. Technol.* **2025**, *10*, 2401920.
21 Farooq, A.; Wanyan, H.; Li, Q.; Lu, S.; Huang, W.; Waqas, M.; Hong, B.; Huang, L.; Chen, L.; Zhou, X.; Wu, H. An adhesive, antibacterial, conductive zwitterionic cellulose nanofibers-containing hydrogel for flexible strain sensors and super-capacitors. *Carbohydr. Polym.* **2025**, *358*, 123534.
22 Luo, Y.; Yang, Q.; Chen, M.; Long, K.; Su, C.; Li, J.; Huang, M.; Lu, A.; Guo, S. Stretchable, adhesive, conductive hydrogel initiated by liquid metal complex for multi-functional sensing. *Chem. Eng. J.* **2024**, *496*, 153674.
23 Luo, J.; Hu, Y.; Luo, S.; Wang, X.; Chen, S.; Zhang, M.; Jiang, J.; Liu, L.; Qin, H. Strong and multifunctional lignin/liquid metal hydrogel composite as flexible strain sensors. *ACS Sustain. Chem. Eng.* **2024**, *12*, 7105−7114.
24 Rao, Z.; Takayanagi, M.; Nagaoka, M. Verification for temperature dependence of tacticity in polystyrene radical polymerization with the combination of reaction pathway analysis and red moon methodology. *J. Phys. Chem. B* **2022**, *126*, 5343−5350.
25 Zhang, Y.; Wei, H.; Hua, B.; Hu, C.; Zhang, W. Preparation and application of the thermo-/pH−/ Ion-Sensitive Semi-IPN hydrogel based on chitosan. *Int. J. Biol. Macromol.* **2024**, *258*, 128968.
26 Yang, L.; Bao, L.; Zhong, Y.; Hao, C.; Chen, J.; Wu, J.; Wang, X. Fabrication of in situ metal-organic framework grown on sodium lignosulphonate hydrogel for removal of Pb2+, methylene blue and crystal violet from aqueous solution. *J. Cleaner Prod.* **2024**, *434*, 139831.
27 Wu, Y.; He, G.; Liu, M.; Huang, L.; Xiang, Y. Epoxy-functionalized coatings *via* free radical polymerization: spray-drying enabled interfacial engineering for high-performance SBR/Kaolin composites. *Prog. Org. Coat.* **2025**, *208*, 109529.
28 Zhang, Y.; Wang, H.; Song, Z.; Wang, C.; Hou, J.; Sui, K.; Qi, P. Directed selective transport and enrichment of micropollutants by gradient hydrogels. *J. Hazard. Mater.* **2025**, *486*, 136929.
29 Jiang, P.; Zhang, Y.; Mu, X.; Liu, D.; Liu, Y.; Guo, R.; Ji, Z.; Wang, X.; Wang, X. Grayscale stereolithography of gradient hydrogel with site-selective shape deformation. *Adv. Mater. Technol.* **2022**, *7*, 2101288.
30 Liu, X.; Liu, S.; Yang, R.; Wang, P.; Zhang, W.; Tan, X.; Ren, Y.; Chi, B. Gradient chondroitin sulfate/poly(γ-glutamic acid) hydrogels inducing differentiation of stem cells for cartilage tissue engineering. *Carbohydr. Polym.* **2021**, *270*, 118330.
31 Jiang, Q.; Shang, Y.; Cheng, H.; Zhao, J.; Yang, L.; He, Z.; Wei, J.; Liang, R.; Su, W.; Zheng, L.; Liao, C. Bioadhesive and antioxidant hydrogel by MoS_2-TA dual-catalytic system initiated free radical polymerization combined with phototherapy for cartilage regeneration. *Mater. Today Bio* **2025**, *33*, 102056.
32 Wang, J. T.; Pei, Y. Y.; Han, B. J.; Sun, R. S.; Zuo, R. T.; Cui, G. X.; Zhang, H.; Cao, Z. Z.; Jin, L.; Li, Q. F. Multifunctional chitosan-based lanthanide luminescent hydrogel with stretchability, adhesion, self-healing, color tunability and antibacterial ability. *Int. J. Biol. Macromol.* **2024**, *264*, 130768.
33 Jia, Z.; Lv, X.; Hou, Y.; Wang, K.; Ren, F.; Xu, D.; Wang, Q.; Fan, K.; Xie, C.; Lu, X. Mussel-inspired nanozyme catalyzed conductive and self-setting hydrogel for adhesive and antibacterial bioelectronics. *Bioact. Mater.* **2021**, *6*, 2676−2687.
34 Rudin, A.; Choi, P., In *The Elements of Polymer Science & Engineering*; Elsevier, Waterloo, **2013**, p. 341
35 Viciosa, M. T.; Quiles Hoyo, J.; Dionísio, M.; Gómez Ribelles, J. L. Temperature modulated DSC study of the kinetics of free radical isothermal network polymerization. *J. Therm. Anal. Calorim.* **2007**, *90*, 407−414.
36 Lloyd, E. M.; Feinberg, E. C.; Gao, Y.; Peterson, S. R.; Soman, B.; Hemmer, J.; Dean, L. M.; Wu, Q.; Geubelle, P. H.; Sottos, N. R.; Moore, J. S. Spontaneous patterning during frontal polymerization. *ACS Cent. Sci.* **2021**, *7*, 603−612.
37 Ye, S.; Yong, W.; Xu, J.; Fu, G. Oxygen- *Co* -Thermal driver for constructing integrated anisotropic hydrogels with programmable shape deformation, superior self-healing, and mechanical performance. *Chem. Mater.* **2023**, *35*, 8170−8180.
38 Kinoshita, K.; Takano, Y.; Ohkouchi, N.; Deguchi, S. Free-radical polymerization of acrylic acid under extreme reaction conditions mimicking deep-sea hydrothermal vents. *ACS Omega* **2017**, *2*, 2765−2769.
39 Furuya, T.; Koga, T. Molecular simulation of effects of network structure on fracture behavior of gels synthesized by radical polymerization. *Macromolecules* **2025**, *58*, 3359−3368.
40 Kuang, Y.; Dormidontova, E. E. Pearl-necklace to unimolecular micelle formation by heterograft bottlebrush polymers in solution. *Macromolecules* **2025**, *58*, 1470−1480.
41 Li, H.; Xue, Z. J.; Xue, Y.-H.; Li, Y.; Liu, H. Topological structure evolution of polymer network based on star-shaped multi-armed precursors. *Chinese J. Polym. Sci.* **2025**, *43*, 1240−1252.
42 Hoogerbrugge, P. J.; Koelman, J. M. V. A. Simulating microscopic hydrodynamic phenomena with dissipative particle dynamics. *EPL* **1992**, *19*, 155.
43 Groot, R. D.; Warren, P. B. Dissipative particle dynamics: bridging the gap between atomistic and mesoscopic simulation. *J. Chem. Phys.* **1997**, *107*, 4423−4435.
44 Müller, M.; Katsov, K.; Schick, M. Biological and synthetic membranes: what can be learned from a coarse-grained description *Physics Reports* **2006**, *434*, 113−176.
45 Español, P.; Warren, P. Statistical mechanics of dissipative particle dynamics. *EPL* **1995**, *30*, 191.
46 Warren, P. Dissipative particle dynamics. *Curr. Opin. Colloid In.* **1998**, *3*, 620−624.
47 Groot, R. D.; Madden, T. J. Dynamic simulation of diblock copolymer microphase separation. *J. Chem. Phys.* **1998**, *108*, 8713−8724.
48 Kröger M. Simple models for complex nonequilibrium fluids. *Physics Reports* **2004**, *390*, 453−551.
49 Yue, L.; Zhang, X.; Li, W.; Tang, Y.; Bai, Y. Quickly self-healing hydrogel at room temperature with high conductivity synthesized through simple free radical polymerization. *J. Appl. Polym. Sci.* **2019**, *136*, 47379.
50 Das, D.; Pham, T, T, H.; Noh, I. Characterizations of hyaluronate-based terpolymeric hydrogel synthesized *via* free radical polymerization mechanism for biomedical applications. *Colloid Surface B* **2018**, *170*, 64−75.
51 Monteferrante, M.; Tiribocchi, A.; Succi, S.; Pisignano, D.; Lauricella, M. Capturing free-radical polymerization by synergetic Ab initio calculations and topological reactive molecular dynamics. *Macromolecules* **2022**, *55*, 1474−1486.